Nuclear Engineering and Technology 55 (2023) 156–168

Contents lists available at ScienceDirect

Nuclear Engineering and Technology

journal homepage: www.elsevier.com/locate/net

Original Article

Effectiveness of Ni-based and Fe-based cladding alloys in delaying hydrogen generation for small modular reactors with increased accident tolerance

Alan Matias Avelar [a, *], Fábio de Camargo [b], Vanessa Sanches Pereira da Silva [b], Claudia Giovedi [c], Alfredo Abe [c], Marcelo Breda Mourão [a]

[a] Department of Metallurgical and Materials Engineering, University of São Paulo, Professor Mello Moraes, 2463, São Paulo, SP, Brazil
[b] Amazônia Azul Tecnologias de Defesa S.A., Corifeu de Azevedo Marques, 1847, São Paulo, SP, Brazil
[c] Nuclear and Energy Research Institute, University of São Paulo, Professor Lineu Prestes, 2242, São Paulo, SP, Brazil

ARTICLE INFO

Article history:
Received 4 July 2022
Received in revised form
22 August 2022
Accepted 3 September 2022
Available online 9 September 2022

Keywords:
Nickel alloys
Stainless steel
High-temperature oxidation
Fuel cladding
Hydrogen generation
Accident tolerant fuel cladding

ABSTRACT

This study investigates the high temperature oxidation behaviour of a Ni–20Cr-1.2Si (wt.%) alloy in steam from 1200 °C to 1350 °C by Thermogravimetric Analysis (TGA), Scanning Electron Microscopy (SEM), Energy Dispersive X-ray Spectroscopy (EDS) and X-ray Diffraction (XRD). The results demonstrate that exposed Ni-based alloy developed a thin oxide scale, consisted mainly of Cr_2O_3. The oxidation kinetics obtained from the experimental results was applied to evaluate the hydrogen generation considering a simplified reactor core model with different cladding alloys following an unmitigated Loss-Of-Coolant Accident (LOCA) scenario in a hypothetical Small Modular Reactor (SMR). Overall, experimental data and simulations results show that both Fe-based and Ni-based alloys may enhance cladding survivability, delaying its melting, as well as reducing hydrogen generation under accident conditions compared to Zr-based alloys. However, a substantial neutron absorption occurs when Ni-based alloys are used as cladding for current uranium-dioxide fuel systems, even when compared to Fe-based alloys.

1. Introduction

A critical safety issue on water-cooled nuclear reactors is the Zr-based alloy severe degradation due to its rapid oxidation at high temperature steam [1–6]. Under accident conditions, Zr-based alloys used as fuel cladding react with water at high temperature and release large amounts of heat and hydrogen, whose combustion load may cause loss of containment integrity and disastrous consequences, as in Fukushima accident, in 2011 [5]. Since then, technical challenges related to the development of Accident Tolerant Fuel (ATF) cladding and the need for research to generate data in support of the deployment of these concepts has been discussed [6–12].

The candidate for ATF cladding materials shall enhance the tolerance in accidental conditions by reducing both enthalpy of metal-water reaction and hydrogen generation rate [6–8]. The former is a significant core heat source [7] and the latter is strongly dependent on the cladding temperature [7,8,12]. For instance, the higher is the cladding temperature during the severe accident progression, the faster is the hydrogen generation and more challenging is the scenario for combustible gas control [5].

In 2020, the International Atomic Energy Agency (IAEA) published the results of a coordinated research project related to the analysis of options and experimental examination of fuels for water cooled reactors with increased accident tolerance (ACTOF) [6]. Chrome coated samples showed the best protection for zirconium substrates on steam oxidation tests performed at high temperatures. However, at 1300 °C, the zirconium substrate was oxidized [6]. Furthermore, the main drawback of this solution is the fact that the Zr-based alloy remains in the core, providing poor mechanical properties at high temperatures [7]. Thus, even at design basis Loss-Of-Coolant Accident (LOCA) scenarios, cladding ballooning and burst may occur [7,13]. Considering burst temperature and oxidation resistance, stainless steel cladding may present safety advantages at LOCA scenarios compared to Zr-based alloys [4,14].

Among Fe-based alloys, FeCrAl has garnered interest due to its good oxidation resistance at high temperatures, as a result of the formation of a stable and protective aluminium oxide layer [8–13,15–20]. However, one major drawback at operating temperatures is the unwanted formation of Cr-rich α' precipitates

* Corresponding author.
E-mail address: alanmatiasavelar@gmail.com (A.M. Avelar).

https://doi.org/10.1016/j.net.2022.09.002

within the Fe-rich α matrix [12]. Significant density of these precipitates was observed after neutron irradiation and α′ number density increased with increasing Cr content in these alloys [18]. Catastrophic acceleration of oxidation at temperatures above 1350 °C has been observed during integral and single effect tests of FeCrAl cladding [21,22]. Also, the formation above 1380 °C of a chemically active melt of iron oxide FeO, which penetrates between the grains of fuel pellets, leading to their disintegration was also observed in single experiments with prototypical UO_2 [23]. The Oxide Dispersion-Strengthened (ODS) Fe–12Cr–5Al alloys was able to maintain an alumina layer up to 1400 °C, but the protective oxide layer was failed at 1450 °C [22]. Moreover, the 304L stainless steel also faces rapid oxidation at this temperature range, possibly because of the Fe–FeO *liquidus* at 1370 °C [24].

Nonetheless, FeCrAl cladding performance in Beyond Design-Basis Accident (BDBA) conditions has been evaluated [19,20]. The current FeCrAl oxidation kinetic models [8,15] under predicted the hydrogen production significantly compared to the test results [20]. Thus, more experimental data at high temperature oxidation for different FeCrAl alloys are needed to support the development of new correlations [20].

Safety analyses have shown that ATF cladding candidates can improve safety margins by providing slower hydrogen generation rates and additional grace period to re-establishment of core cooling [6,19,25–27]. The results of severe accident simulations show that although significantly less hydrogen is produced throughout the accident progression, little additional coping time is gained for short-term complete failure of the Emergency Core Cooling System (ECCS) and partially mitigated SBO (Station Blackout) scenarios [25–27]. The usefulness of this additional coping time, which can be minutes or a few hours, depending on the reactor design and accident scenario, needs to be assessed by regulators [7,19,25–27].

Other possibilities for ATF claddings, including Ni-alloys and NiCr coated Zr have been studied [28–32]. Solely, NiCr coatings do not provide protection of Zr-based alloys due to the fast interdiffusion of Ni into the alloy and of Zr into the coating, resulting in the formation of ZrO_2 [28,30]. Taking into account Ni-based alloys as cladding materials, their susceptibility to radiation damage is one of the main challenges [11,31]. Compared to stainless steels, there is less experience with neutron irradiation effects on Ni-based alloys, but available information indicates that the plasticity reduction is comparable with austenitic stainless steel after irradiation [31,33].

Limited information is available on NiCr alloys oxidation as ATF cladding candidate at the onset of BDBA conditions [34–36]. If a minimal amount of alloy is oxidized and the cladding is capable to maintain its mechanical integrity, it might be considered as an ATF candidate. Thus, it is desirable to determine oxide growth kinetics in short-term periods, in order to assess the effectiveness of Ni-based cladding in delaying fuel degradation in water cooled reactors at BDBA.

In this study, the oxidation of a Ni–20Cr-1.2Si (wt.%) alloy in steam from 1200 °C to 1350 °C is investigated. The results were compared with the behaviour of Zr-based and Fe-based alloys. The oxidation kinetics were applied into a simplified core model [27] to assess the hydrogen generation evolution of a LOCA without ECCS on a hypothetical Small Modular Reactor (SMR).

2. Experimental procedure

2.1. Sample preparation

Ni-based alloy samples were cut from a plate into small discs, with initial mass around 8 g, 25 mm of diameter, and 2 mm of thickness and the surface was prepared by polish process with SiC grinding paper up to #600 mesh. The chemical compositions were determined by Energy Disperse X-ray (EDX – Shimadzu model 800HS), Inductively Coupled Plasma Optical Emission Spectrometry (ICP-OES – PerkinElmer model AVIOS 500) for majors (>0.1 wt %) and minors (<0.01 wt%) elements, respectively, and the direct combustion method for carbon and sulphur (C/S Analyzer Eltra model CS-2000). The chemical composition results are summarized in Table 1.

2.2. High temperature steam oxidation and characterization

Thermogravimetry Analysis (TGA) was applied to evaluate the oxidation kinetics by measuring Weight gain (Wg) evolution throughout the test. Prior to the experiment, samples were weighed two times using a Shimadzu AUY220 analytical balance with 0.1 mg resolution and the average weight was calculated for each specimen. During the test, mass gain was measured at 20, 60, 180 min, and after it, each oxidized sample was weighed two times using the same procedure.

A high temperature oxidation apparatus with a Lindberg/Blue electric furnace and a steam generator to produce pure flowing steam was set up. Steam was generated by pumping distillate water from a reservoir placed underneath the furnace into a steam generator, which was heated by a Quimis heating plate. Water was pumped using an Ismatec peristaltic pump giving approximately 1.3 ml/min. In the furnace, steam flowed into the hot zone, passing over the sample, which was positioned using an alumina crucible suspended by a platinum wire hook attached to the bottom of the Shimadzu analytical balance mounted above the furnace. The alumina crucible allowed catching possible scale spalling of non-adherent oxide layer. Fig. 1 describes the experimental apparatus schematically.

Before the tests, furnace temperature verification was carried out in order to determine the hot zone and set the experimental temperature on the sample. Steam flow markedly affected the results at the order of the weight scale resolution, especially at 1200 °C. Thus, it was necessary to perform kinetic measurements by discontinuous method as a significant noise was observed in the continuous weight gain curve. Steam flow was switched-off for a few seconds to allow weight gain measurements at previously specified periods throughout the 180 min test.

Oxidation conditions were selected considering BDBA temperatures [6], where accident tolerance is to be analysed. Oxidation times considered the short coping time of cladding after the onset of oxidation [26]. Prolonged tests (180 min) were carried out in order to avoid extrapolation of initial results, which might have led to erroneous interpretations.

Table 2 presents the experimental investigations. It is worthwhile mentioning that every experiment was performed three times. After oxidation, the steam flow was switched off and the sample was cooled down to room temperature in nitrogen flow to avoid additional oxidation during cooling.

Surfaces and cross sections of the exposed samples were investigated by Scanning Electron Microscopy (SEM), Energy Dispersive Spectroscopy (EDS), and X-ray Diffraction (XRD). EDS line scan was used to assess the diffusion of alloying elements and

Table 1
Chemical composition of Ni-based alloy (wt.%, balance Ni) used in high temperature steam oxidation experiments.

Cr	Si	Nb	Al	Fe	C	B
19.30	1.18	0.69	0.16	0.15	0.083	0.069
Ti	Ca	P	Mn	Co	Cu	S
0.058	0.036	0.032	0.027	0.016	0.003	0.003

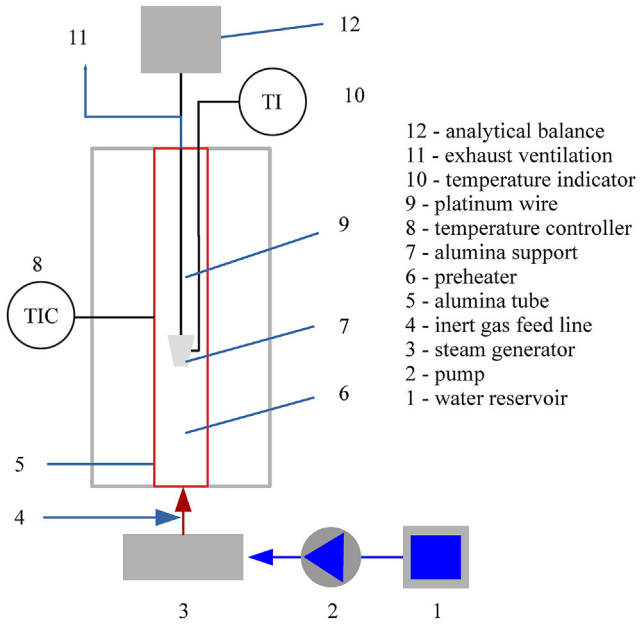

Fig. 1. Schematic arrangement of steam oxidation test furnace.

Table 2
Summary of experimental high temperature steam oxidation.

Test	Temperature [°C]	Time [min.]
1	1200	20
2	1300	20
3	1350	20
4	1200	60
5	1300	60
6	1350	60
7	1200	180
8	1300	180
9	1350	180

their concentration in the oxidized region in comparison to the bulk material. XRD was applied to analyse scales and bulk phases.

3. Modelling approach

In order to gain deeper understanding of the material behaviour as fuel-cladding during an accident scenario, materials properties, including their oxidation kinetics were applied into a simplified numerical core model developed using Visual Basic for Applications (VBA), entitled SMR model [27]. Numerical investigations allow rapid evaluations of different single effect models under multiple effects conditions, without the need to access sophisticated severe accident computer codes [27,37].

The adopted model considers the core of a water cooled reactor consisting of a number N_R of fuel rods. The active height of the reactor core is L. The volumetric heat generation rate of each fuel rod is given by the decay heat power as a function of time in accordance with ANSI/ANS 5.1–2014 [38]. The temperature evolution in the core is determined by solving the transient heat conduction equations for fuel and cladding, expressed in Eqs. (1) and (2), respectively.

$$\frac{1}{r}\frac{\partial}{\partial r}\left(rk_f(T)\frac{\partial T_f^i(r,z,t)}{\partial r}\right)+\frac{\partial}{\partial z}\left(k_f(T)\frac{\partial T_f^i(r,z,t)}{\partial z}\right) + q_f^i(z,t)=\rho_f Cp_f\frac{\partial T_f^i(r,z,t)}{\partial t},\ 0<r<R_{fo},\ 0<z<\frac{L}{2}, i=1,\ldots,N_R \tag{1}$$

$$\frac{1}{r}\frac{\partial}{\partial r}\left(rk_c(T)\frac{\partial T_c^i(r,z,t)}{\partial r}\right)+\frac{\partial}{\partial z}\left(k_c(T)\frac{\partial T_c^i(r,z,t)}{\partial z}\right) + q_c^i(z,t)=\rho_c Cp_c\frac{\partial T_c^i(r,z,t)}{\partial t},\ R_{ci}<r<R_{co},\ 0<z<\frac{L}{2}, i=1,\ldots,N_R \tag{2}$$

where the outer radius of the fuel pellet, inner and outer radius of the cladding are R_{fo}; R_{ci} and R_{co}, respectively. T_f^i and T_c^i are temperatures, ρ_f^i and ρ_c^i are densities, Cp_f^i and Cp_c^i are specific heat, k_f^i e k_c^i are thermal conductivities, q_f^i e q_c^i are volumetric heat generation of fuel and cladding, respectively, for the i-th fuel rod.

The axial profile of volumetric heat generation rate at i-th fuel rod is given by Eq. (3).

$$q_f^i(z,t)=q_f^i(t)\cdot\left(\frac{\pi}{2}\right)\cdot\cos\left(\frac{\pi z}{L}\right) \tag{3}$$

Axial symmetry was applied and simulations considered only half of the oxidation area. Thus, the final hydrogen generation was multiplied by a factor of 2. Axial limits and symmetry, such as radial symmetry were also considered adiabatic. Equations from (4) to (7) present radial boundary conditions and from Eq. (8) to Eq. (11) present axial boundary conditions for both fuel and cladding domains.

A complete dry-out condition is applied to provide a conservative hydrogen generation during accident progression. The complete dry-out condition is applied during refill and during reflood phases of LOCA, where heat transfer calculations shall be based on the assumption that cooling is only by steam. Instead, in this study, an adiabatic boundary was imposed on the outer surface of the cladding.

$$\left.\frac{\partial T_f^i(r,z,t)}{\partial r}\right|_{r=0}=0 \tag{4}$$

$$\left.-R_{fo}k_f\frac{\partial T_f^i(r,z,t)}{\partial r}\right|_{r=R_{fo}}=R_g h_g\left(T_f^i\left(R_{fo},z,t\right)-T_c^i(R_{ci},z,t)\right) \tag{5}$$

$$\left.-R_{ci}k_c\frac{\partial T_c^i(r,z,t)}{\partial r}\right|_{r=R_{ci}}=R_g h_g\left(T_f^i\left(R_{fo},z,t\right)-T_c^i(R_{ci},z,t)\right) \tag{6}$$

$$\left.-k_c\frac{\partial T_c^i(r,z,t)}{\partial r}\right|_{r=R_{co}}=0 \tag{7}$$

$$\left.-k_f\frac{\partial T_f^i(r,z,t)}{\partial z}\right|_{z=0}=0 \tag{8}$$

$$\left.-k_f\frac{\partial T_f^i(r,z,t)}{\partial z}\right|_{z=\frac{L}{2}}=0 \tag{9}$$

$$\left.-k_c\frac{\partial T_c^i(r,z,t)}{\partial z}\right|_{z=0}=0 \tag{10}$$

$$\left.-k_c\frac{\partial T_c^i(r,z,t)}{\partial z}\right|_{z=\frac{L}{2}}=0 \tag{11}$$

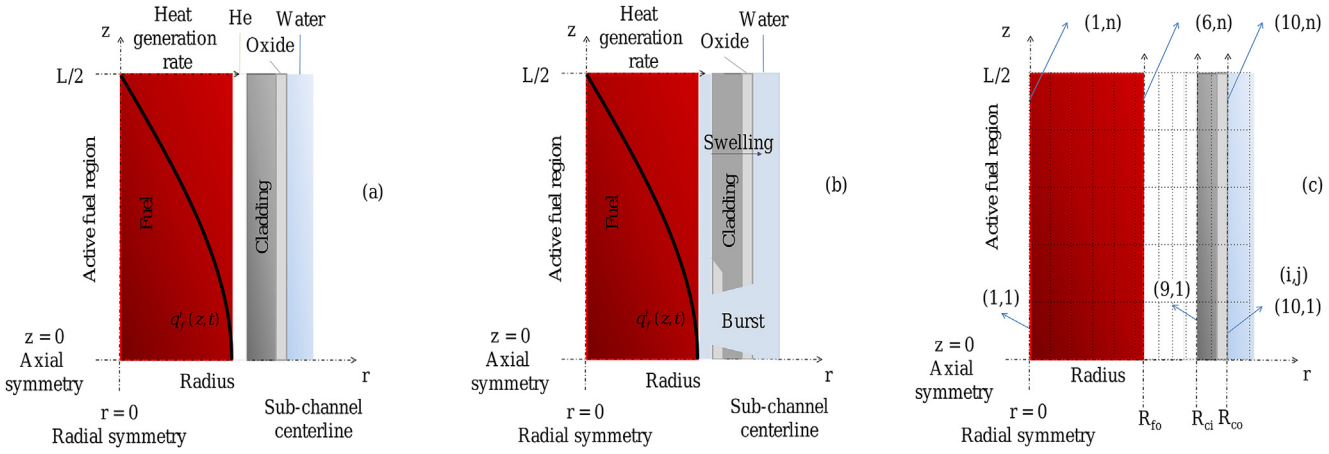

Fig. 2. Fuel rod simplified model considering (a) axial heat generation rate from decay heat, (b) ballooning creep strain, burst and inner cladding area oxidized after cladding rupture (c) finite difference nodal points.

The gap heat transfer h_g was calculated according to Eq. (12) [37].

$$h_g = \frac{k_g}{\left(R_{ci} - R_{fo}\right)} + \frac{\sigma_{SB} \cdot \left(T_{fo}^2 + T_{ci}^2\right) \cdot \left(T_{fo} + T_{ci}\right)}{\left(\frac{1}{E_f} + \frac{R_{fo}}{R_{ci}} \cdot \left(\frac{1}{E_c} - 1\right)\right)} \tag{12}$$

where σ_{SB} is the Stefan-Boltzmann constant, E_f is fuel emissivity and E_c cladding emissivity. Gap was considered to be filled with He, whose thermal conductivity was calculated in accordance with applicable correlations [39].

As the code calculates the temperature distribution within the cladding by finite difference method, a grid independence test was performed for the smallest number of cells (elements) with less than 2% difference in the numerical results of hydrogen generation. Once the temperature distribution in the fuel and cladding of all fuel rods in the reactor core are determined, hydrogen generation rates due to metal-water reaction were calculated, assuming that reaction is not steam limited. For rods whose cladding rupture occurred during LOCA, part of the inner cladding area was assumed to react after the rupture. Fig. 2 ilustrates the fuel rod model's considering (a) heat generation rate axial profile, (b) inner cladding oxidation due to burst and (c) finite difference nodal points.

The general rate law equation for oxide mass gain is represented by Eq. (13). If n equals 2, the growth of the oxide layer follows a parabolic rate, for example.The reaction rate constant k is a thermally dependent parameter and follows an Arrhenius relationship, as given by Eq. (14).

$$\left(\frac{\Delta w}{A}\right)^n = k \cdot t \tag{13}$$

$$k = A_0 \cdot \exp\left(-\frac{E_A}{R \cdot T}\right) \tag{14}$$

where $\frac{\Delta w}{A}$ is mass-gain per unit area; t is time, A_0 is pre-exponential factor; E_A is the activation energy of the oxidation reaction; R is the universal gas constant and T is temperature in kelvin.

The mass gain data were used to derive hydrogen generation rate for these materials, by using stoichiometric relations [4,27], as given by Eq. (15).

$$\dot{m}_{H2} = 2 \cdot \frac{M_{H_2}}{M_{O_2}} \cdot \sqrt[n]{A_0 \cdot \exp\left(-\frac{E_A}{R \cdot T}\right)} \cdot t^{(1/n)-1} \cdot \frac{1}{n} \tag{15}$$

where $\dot{m}_{H2}$ is hydrogen generation rate per area; M_{H_2} and M_{O_2} are the molecular weights of hydrogen and oxygen, respectively; and 2 is the number of hydrogen moles produced for each mole of oxygen reacted.

Cladding swelling and rupture were calculated according to Yadav (2018) model [37] for Zr-based cladding. On the other hand, cladding ballooning due to creep was considered negligible for Fe-based alloys [13]. Mechanical and thermal properties of the alloys were obtained from available literature [39–44]. For Zr-based alloys at high temperatures, dislocation climb induced creep is dominant mechanism of deformation in β-phase of Zr-based alloys [37] and the code calculates the creep strain by the time integration of the power law-Arrhenius equation for a steady state creep rate.

The circumferential strain at each time step was applied to calculate instantaneous tangential stress. As the deformation was quite large near burst, to improve the prediction of stress at burst, the code was switched to a smaller time step [37]. Instantaneous stress was compared to burst stress at the calculated cladding temperature in order to verify the possibility of rupture. Burst stress criteria applied for Zr-based and 304 stainless steel are taken from Refs. [13,37], respectively.

High temperature creep behaviour of Ni-based alloys have been studied by several authors [45–48]. However, to the best of the authors knowledge, data on burst temperature and hoop stress of thin walled Ni-based fuel rod cladding are not available. Further investigation is necessary to assess burst behaviour of Ni-based alloys [44].

After burst, steam flows into the gap. Then, heat transfer coefficient starts to consider steam thermal conductivity [39] instead of He. If *liquidus* temperature is achieved, remaining hydrogen source term from cladding oxidation is considered to be released instantaneously. Fig. 3 presents a simplified code flowchart.

Other phenomena such as axial thermal strain and volume expansion due to the scale growth (also known as Pilling-Bedworth ratio – PBR) were not considered in the model. The adiabatic boundary condition already provides better degree of conservativeness rather than heat conduction through additional volume.

The SMR model developed based on the NuScale Power Module (NPM) [49] was applied to predict hydrogen generation up to start of core melting of different fuel claddings during a hypothetical

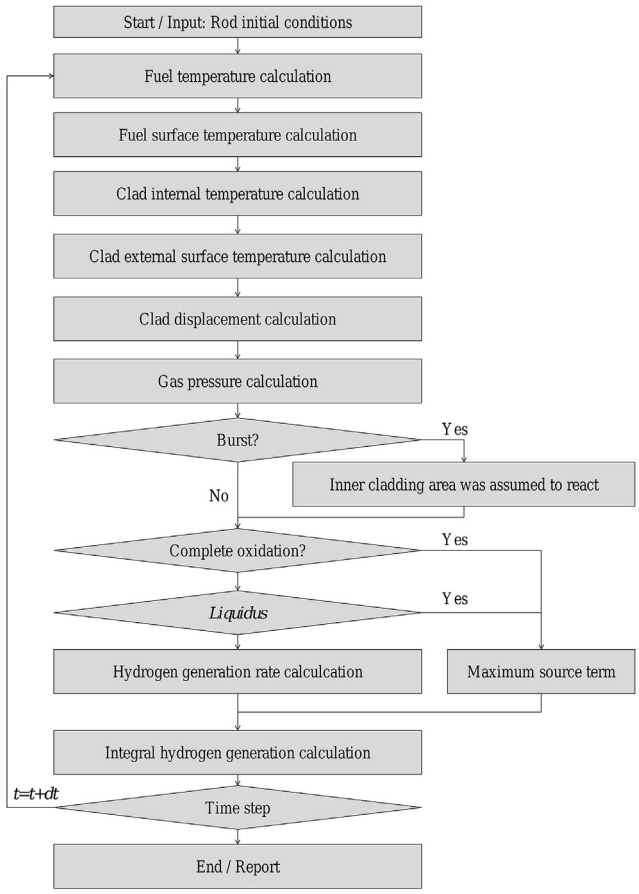

Fig. 3. Simplified code flowchart.

unmitigated LOCA scenario. Simulation time started at the onset of complete core dry-out and it was defined as the maximum period in which Peak Cladding Temperature (PCT) is below the alloy's *solidus* temperature, when cladding material starts to melt. The main NuScale reactor core design parameters are given by Table 3 [49]. Thermophysical properties of materials were obtained from databases [40–42,50]. The initial power is 163.2 MWt, 102% of the reactor nominal power. The code main assumptions and simplifications are as follows:

- The heat generation rates from radioactive decay of fission products is assumed to be equal to 1.2 times the values for infinite operating;
- The degree of swelling and rupture is taken into account in calculation of cladding oxidation and hydrogen generation;
- Heat transfer calculations are based on the assumption that fuel rods have no cooling (adiabatic boundary condition); and
- Metal-water reaction is assumed not to be steam limited.

4. Results and discussion

4.1. Thermogravimetric Analysis

Weight gain (Wg) measurements by discontinuous method were obtained for each oxidized sample at 20, 60, and 180 min. Results evidenced that weight gain increased gradually with increasing temperature and with exposure time. The growth of Cr_2O_3 scale is governed by a diffusion-limited growth mechanism

Table 3
NuScale Power Module reactor core design parameters [49].

Parameter	Value
Thermal power	160 MW
Fuel Assembly Type	17 x 17
Fuel rod outside diameter	0.374 in (9.50 mm)
Cladding thickness	0.024 in (0.61 mm)
Active fuel column length	78.74 in (2.00 m)
Fuel rod pitch	0.496 in (12.5984 mm)
Fuel pellet diameter	0.3195 in (8.1153 mm)
Fuel pellet length	0.4 in (10.16 mm)
Pellet-cladding diametral gap	0.0065 in (0.1651 mm)
Fissile enrichment	4.45%
Fuel pellet density (%theoretical density)	96.0
Total number of fuel rods in core	9768
Radial ring A peaking factor	0.883
Radial ring B peaking factor	0.886
Radial ring C peaking factor	0.915
Radial ring D peaking factor	0.980
Radial ring E peaking factor	1.105
Radial ring F peaking factor	1.029
Radial ring G peaking factor	1.003
Radial ring H peaking factor	1.064
Radial ring I peaking factor	1.123

[51]. Thus, the first attempt was to evaluate the assumption that the weight gain values would obey parabolic kinetics. However, the experimental data showed significant deviation from such fit. On the other hand, the oxidation kinetics were reasonably fitted with a power law by plotting weight gain results and time in log scale. The better description of the oxidation kinetics would be a quartic law, accordingly to Eq. (13) considering n = 4. Fitting curves are shown in Fig. 4, where experimental quartic reaction rate constants (k_q) were obtained by linear regression.

It seems volatilization of the oxide scale still played a role in the oxidation process [51]. Thus, as time goes by, the typical parabolic behavior is not followed due to the volatilization of specimens. Although the investigation of oxidation kinetics was performed with limited data points and at relatively short time oxidation, results systematically show a significant increase on the oxidation resistance compared to currently employed cladding alloys [4]. The volatilization can help explain chromium coated samples at high temperatures presented systematic differences between hydrogen mass and sample mass gain [6].

The Arrhenius plot was built as shown in Fig. 5. The linear fit obtained by this plot shows that the dependence of the calculated quartic reaction rate constant k_q with temperature agrees with Arrhenius relationship presented in Eq. (14).

Thus, the experimental data yielded the following quartic oxidation kinetics presented in Eq. (16) for NiCr alloy containing Si in short-term high temperature oxidation by steam. A similar quartic oxidation kinetics was observed for Cr coatings in steam environments at high temperatures [51].

$$\frac{\Delta w}{A} = \sqrt[4]{\left(1.97 \cdot 10^{35} \cdot \exp\left(\frac{-110000 \pm 6900}{T}\right) \cdot t\right)} \tag{16}$$

where $\frac{\Delta w}{A}$ is mass-gain per unit area [mg/dm^2]; t is time [min.] and T is temperature [K].

Other researchers have shown for oxidation of Cr coatings at temperatures up to 1300 °C that the overall oxidation kinetics is nearly parabolic at the beginning of oxidation, when the Cr outer layer is protective [52]. However, in general, calculations indicate that the oxidation kinetics of Cr coating does not follow a parabolic or quartic law perfectly [53]. Although the oxidation rate of the Cr coating is lower when in comparison with that of the Zr, Cr and Zr

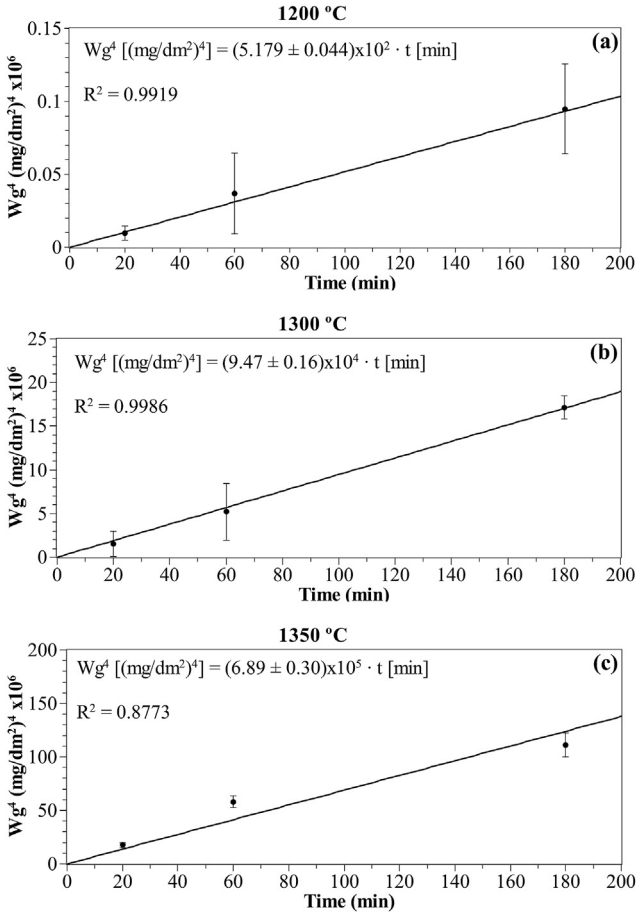

Fig. 4. Experimental weight gain curves of Ni–20Cr-1.2Si steam oxidation at (a) 1200 °C, (b) 1300 °C, and (c) 1350 °C. The data points were fitted by quartic law.

could inter-diffused to form a Cr–Zr layer. Thus, the outward diffusion of Zr along chromium grain boundaries promotes further inward oxygen diffusion [52].

It is possible to compare weight gain data as a function of exposure time for the Ni–20Cr-1.2Si specimen at 1200, 1300, and 1350 °C in steam to the prediction given by the kinetic model presented in Eq. (16). The correlation between the model proposed here and the experimental data is shown in Fig. 6.

Comparing to austenitic stainless steel such as AISI 304L and 348, Ni-based alloys present better oxidation resistance at high temperatures [4]. In fact, Ni–20Cr-1.2Si specimen met the ATF criteria of 100x in oxidation resistance in steam at 1200 °C for short

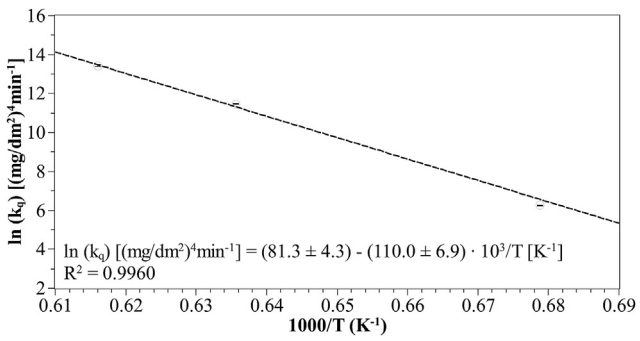

Fig. 5. The Arrhenius plot of quartic reaction rate constant.

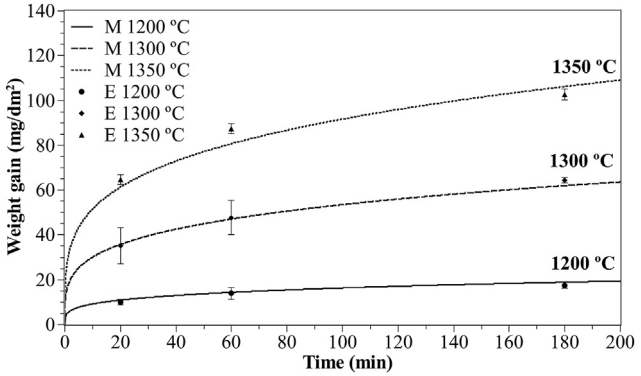

Fig. 6. Weight gain curves for quartic law kinetic model (M) of Ni–20Cr-1.2Si oxidation at 1200 °C, 1300 °C, and 1350 °C in steam compared with mean experimental measurements (E).

times compared to Zr-based alloys improvement (i.e. less than Zr-based alloy value divided by 100) [8]. Table 4 presents the weight gains of Zr-based, Fe-based, and Ni-based specimens in steam at 1200 °C after 20 and 60 min of exposure [1,2,4,23].

The significant lower weight gains observed for Ni–20Cr-1.2Si specimen correspond to approximately 0.4% and 0.3% at 20 and 60 min of the calculated oxidation of Zr-based alloys, respectively. Moreover, other studies have reported higher weight gain for uncoated Zr-based alloys samples at high temperature steam oxidation. For example, more than 75 mg/cm^2 after 60 min at 1200 °C, and more than 45 mg/cm^2 after 20 min at 1100 °C [28,29].

Although discontinuous method was applied, no breakaway or any abrupt change in oxidation rate was observed in the experiments. Therefore, ATF cladding performance oxidation criteria may be considered as accomplished. Ni-based materials were already studied for high temperature reactor systems [48] and nowadays, Ni-based alloys are currently under consideration as a cladding for an accident tolerant fuel [31,50].

The high oxidation resistance observed for NiCr alloys reflects, as it will be presented in the next section, not only the formation of Cr_2O_3 but also an inner SiO_2 layer identified through different characterization techniques. The addition of Si is said to improve oxidation resistance of NiCr alloys, due to low diffusion of chromium and nickel through SiO_2 [35].

4.2. Characterization

Exposure of Ni–20Cr-1.2Si alloy at high temperature steam resulted in surface morphological changes in the samples. Fig. 7 presents visual inspection of as prepared and oxidized samples surfaces. The metallic appearance of the samples before the test (Fig. 7 (a)) changed into a grey oxide or dark green (Fig. 7 (b) and (c)), which is typical of the formation of chromium and nickel oxides on the surface after oxidation tests [30,51].

Ni–20Cr-1.2Si alloy showed significant oxidation resistance in steam when compared to AISI 348. Indeed, photographed oxidized samples presented a much better performance compared to Zr-based and Fe-based alloys from previous studies [4], even for an extended oxidation period of 3 h.

As shown in Fig. 7 (f), Zr-based alloys may present pronounced loss of mechanical properties at BDBA temperatures [1–4]. Austenitic stainless steel might present significant scale spalling [4], as shown in Fig. 7 (e). On the other hand, Ni-based alloys may provide increased accident tolerance for water cooled reactors, as presented in Fig. 7 (d).

The lower quantity of debris generated by the Ni-based alloys

Table 4
Weight gain calculated for Zr-based, Fe-based and observed for Ni-based alloys after 20 min and 1 h steam oxidation at 1200 °C [1,2,4,23].

Time [min.]	Category of alloy	Weight gain [mg/cm^2]	Reference
20	Zr-based	28.65	Avelar et al. (2020) [4]
		30.03	Baker and Just (1962) [1]
		22.82	Cathcart et al. (1977) [2]
	Fe-based	19.01	Avelar et al. (2020) [4]
		29.62	Bittel et al. (1969) [24]
	Ni-based	0.099 ± 0.012	This study
60	Zr-based	49.63	Avelar et al. (2020) [4]
		52.01	Baker and Just (1962) [1]
		39.53	Cathcart et al. (1977) [2]
	Fe-based	52.17	Avelar et al. (2020) [4]
		51.30	Bittel et al. (1969) [24]
	Ni-based	0.139 ± 0.026	This study

would reduce significantly the amount of particulates during reactor reflood relative to Zr-based and Fe-based alloys, as shown in Fig. 7 (d)–(f) [4,6].

Characterization of the oxidized samples layers has been carried out using SEM, EDS, and XRD techniques, where discontinuous oxide multilayers were observed, besides voids. The results systematically indicated that a silica layer was formed at the oxide-metal interface. Fig. 8 shows the cross-section morphology and EDS maps for the Ni–20Cr-1.2Si specimen after 20 min oxidation at 1200 °C.

According to Douglas and Armijo [35] the addition of Si to Ni–20Cr reduces oxidation rate at high temperature conditions. The oxidation of Ni–Cr alloy containing Si was also characterized by the formation of SiO_2 in the scales between the alloy and the layer of Cr_2O_3, as shown in Fig. 9 and Fig. 10.

Composition of SEM points of Ni–20Cr-1.2Si alloy that was oxidized at 1350 °C was also analysed and these results are presented in Fig. 10. Points 1–3 were heavily oxidized, and points 6 and 7 were the non-reacted. Cr and Si gradients toward the outer surface gradually changes at the heavily oxidized points, especially from point 3 to point 1. Points 6 and 7 show the enrichment of Ni due to the diffusion of Cr and Si towards the oxide layer.

Due to the low solubility of Cr and Ni in SiO_2 there is very little chemical potential (driving force) for diffusion of such elements through SiO_2 [35]. So, the formation of a SiO_2 layer at the oxide-metal interface is responsible to increase the oxidation resistance in steam, despite the possibility reported by previous studies that SiO_2 layer at oxide-metal interface may lead to slight spalling [35,54], where no breakaway oxidation took place, due to the growth stress between the SiO_2 layer and the alloy.

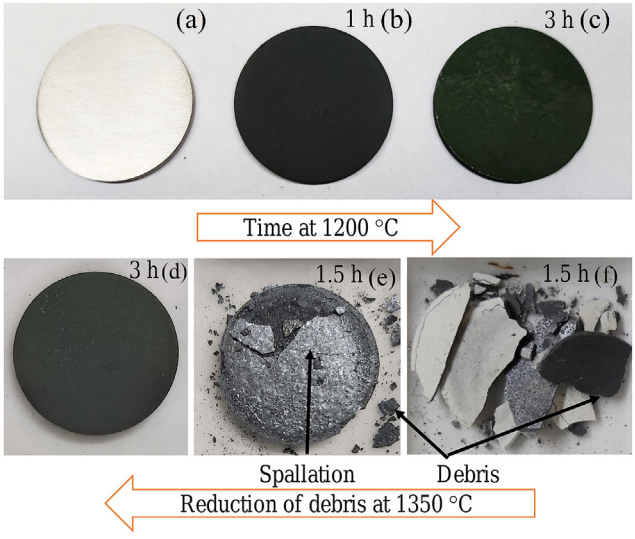

Fig. 7. Photographs of Ni–20Cr-1.2Si samples surfaces (a) as received, and after (b) 1 h of oxidation and (c) 3 h of oxidation by steam at 1200 °C, and a comparison of (d) Ni–20Cr-1.2Si after 3 h at 1350 °C against (e) AISI-348 and (f) Zr-4 after 1.5 h of oxidation by steam at the same temperature.

On the other hand, austenitic stainless steels, such as AISI 348, are not able to sustain accident conditions for prolonged periods. Fig. 11 (a) shows that the growth of Fe oxides indicates the lack of Cr availability in the outer layer [4]. Therefore, while in NiCr, the high Cr content protects the oxidation of Ni, the opposite behaviour is seen for AISI 348, where the analysis of the outer layer by Raman spectroscopy revealed only magnetite, which indicates lack of protection; see Fig. 11 (b).

XRD patterns of the as received and oxidized Ni–20Cr-1.2Si samples are shown in Fig. 12 (a). The reflections of a face centered cubic (fcc) structure correspond to NiCr substrate. For the oxidized sample at 1200 °C, the oxides formed are composed basically by Cr_2O_3 and SiO_2 as shown in Fig. 12 (b). The spinel structure ($NiCr_2O_4$) is hardly detected at these temperatures. However, at 1300 °C and 1350 °C the presence of a spinel type of M_3O_4 is undoubted, as can be seen at Fig. 12 (c) e (d) respectively.

According to Ref. [35], although Cr was preferentially oxidized to form a Cr_2O_3 layer, initially the large Ni availability at metal surface leads to NiO formation, then the beneath Cr-enriched surface alloy tends to form chromium(III) oxide.

As the solubility of Ni in Cr_2O_3 is very small, very little diffusion of Ni took place through the Cr_2O_3 layer. Therefore, the growth of NiO is quickly mitigated, which may be the reason for the lower evidence of Ni presence in the oxide layer as shown in Fig. 8 and in Fig. 9, where it is not possible to see a Ni signal on oxide layer. Moreover, NiO can react with Cr_2O_3 forming $NiCr_2O_4$ thin layers [35,55], which was identified by XRD, as can be seen in Fig. 12.

After this state, the Cr_2O_3 layer growths, and turns the major product. The outer spinel layer formed offered little protection as it readily spalled off during metallographic preparation [35,54,55]. Tests conducted at higher temperature, such as 1350 °C, provided conditions for a faster kinetic formation of Cr_2O_3 layer, with a SiO_2 thicker layer at the interface oxide-alloy. Comparing the XRD results presented in Fig. 12 for 1300 °C (c), and 1350 °C (d) it is possible to confirm the higher growth of this duplex layer by looking at the inversion of the dominant phase from NiCr alloy to Cr_2O_3. Meanwhile, the sign observed for SiO_2 appears approximately the same, despite of the greater attenuation promoted by thicker Cr_2O_3 outer layer.

Based on the experimental results, Fig. 13 presents the short-term oxidation mechanism of Ni–20Cr-1.2Si in steam at high temperatures and water dissociation reactions that may occur. After the possible first NiO formation, the water-metal reactions occur

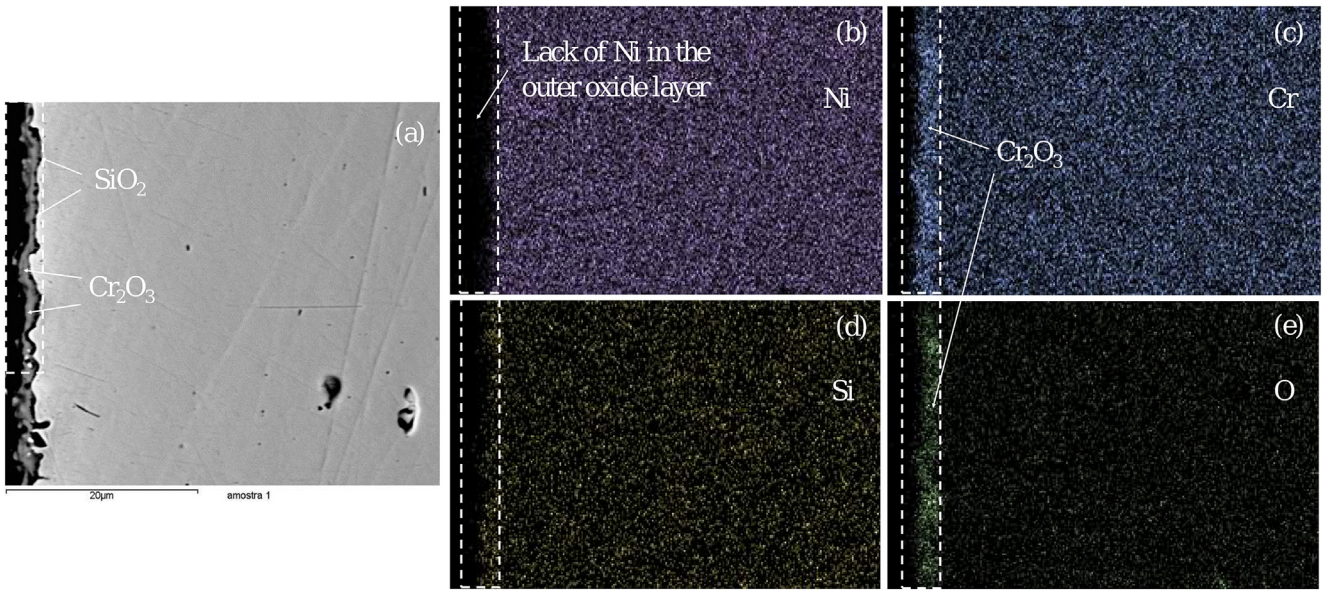

Fig. 8. (a) Cross-section backscattered electrons (BSE) SEM image of the Ni–20Cr-1.2Si specimen after 20 min oxidation at 1200 °C and EDS maps for (b) Ni, (c) Cr, (d) Si, (e) O, with the outer oxide layer highlighted.

at the interface of metal and initial chromium(III) oxide scale is created [35], while below this layer silica starts to nucleate. A dual oxide layer comprised of Cr_2O_3 and SiO_2 was also observed on the oxidation of FeCrSi alloys with high Cr content (≥16% Cr) [56], but none spinel structure was identified for Fe–20Cr–2Si alloy [56]. Similar diffusion-volatilization mechanism can be applied for NiCrSi.

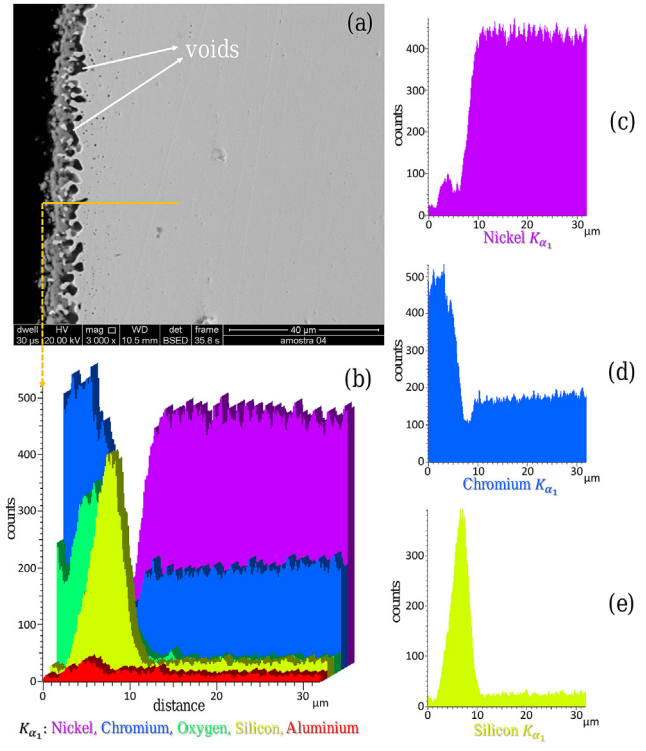

Fig. 9. (a) Cross-section BSE SEM image of the Ni–20Cr-1.2Si specimen after 60 min oxidation at 1350 °C and (b) EDS line scans of main alloying elements with separated profiles of (c) Ni, (d) Cr, and (e) Si.

The Cr_2O_3 layer in oxide scale will generate hydroxide in steam, and volatilize gradually in the form of $CrO_2(OH)_2$ [56], which helps explain the quartic kinetics [51]. SiO_2 still grows between the metal-Cr_2O_3 interface, despite of Si/Cr volatilization and the increasing attenuation of the outer Cr_2O_3 layer. This is possible due to volatilization, since there might not be Cr_2O_3 above SiO_2 or water could reach SiO_2 through cracks. In this phase voids are left from volatilization, especially at high temperatures [56], as presented in Figs. 9 and 10.

Third, the increase of growth stress between the SiO_2 inner layer and the alloy occur, as cracks are observed between oxide scale and substrate. This may be attributed due to the difference of SiO_2 layer and alloy in terms of thermal expansion coefficient [54]. This difference resulted in scale spalling at the interface of SiO_2 layer and the alloy. As the scale spalls off, exposed area experiences oxidation again. However, the diffusion of Cr was fast enough to avoid significant oxidation of Ni, despite significant Cr volatilization.

4.3. Performance assessment and discussion

4.3.1. Performance assessment

In order to assess the performance of different cladding materials, the simplified reactor core model was applied to predict hydrogen generation up to start of melting in an unmitigated LOCA without ECCS scenario. Simulation results were computed here up to the point where Peak Cladding Temperature (PCT) reached the alloy *solidus* temperature. The temperature range that ATF alloys faces rapid oxidation is close to their *liquidus* temperature [26]. Thus, they tend to relocate rather than to undergo excessive oxidation. Consequently, part of these alloys might leave the reactor pressure vessel in a molten state without oxidizing.

For Zr-based alloys, *solidus* and *liquidus* temperatures were considered the same [57]. Fe–FeO *liquidus* temperature was considered for Stainless Steel (SS) case [58]. The threshold temperature for steam attack was applied for FeCrAl case [26]. Nickel–Chromium alloy 42KhNM properties were applied to NiCr case [44]. Metal-water reactions heat generation were calculated considering the enthalpy of formation of substances at 298 K [59]. Table 5 summarizes the main properties and simulation results.

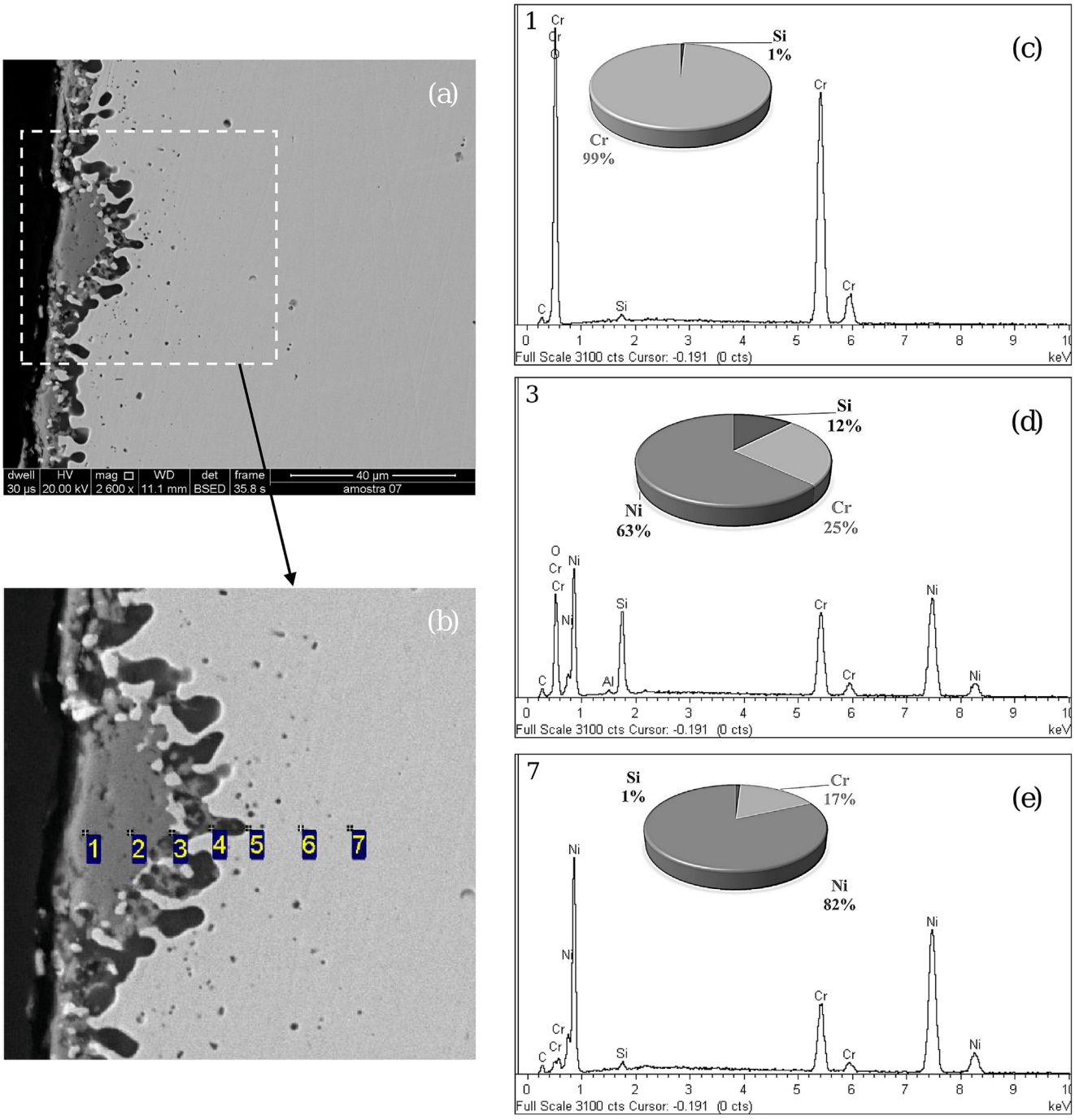

Fig. 10. (a) Cross-section BSE SEM image of the Ni−20Cr-1.2Si specimen after 180 min oxidation at 1350 °C, (b) composition points scans, EDS spectra and normalised results in weight % of (c) point 1, (d) point 3, and (e) point 7.

Although FeCrAl does not have the highest melting temperature, it is the last cladding to start melting among the ATF candidates. The lower absolute enthalpy of metal-water reaction and the oxidation resistance may explain its better performance. NiCr alloy presented the lowest hydrogen production up to the start of core melting. Fig. 14 (a) presents PCT evolution up to the start of melting and Fig. 14 (b) the total hydrogen generated for different cladding alloys.

Fig. 14 (a) shows the effect of Zr-water highly exothermal reaction on accelerating core heat-up, which promoted an increasingly faster heating rate (6 K/s) because of the accelerated oxidation. Thus, despite presenting the higher melting temperature, Zr-based alloys are likely to melt before other ATF candidates. Thus, ATF candidates provide additional coping time to the re-establishment of core cooling. Fig. 14 (b) shows that ATF cladding delay hydrogen generation compared to Zr-based cladding. This would provide a less challenging scenario to combustible gas control systems and less heat to be removed by emergency core cooling system.

In order to take into account the catastrophic oxidation of FeCrAl due to the formation of the FeO melt at 1375°C (586 s), another calculation was performed considering the kinetics of stainless steel oxidation to represent FeCrAl behaviour above 1375°C [26].

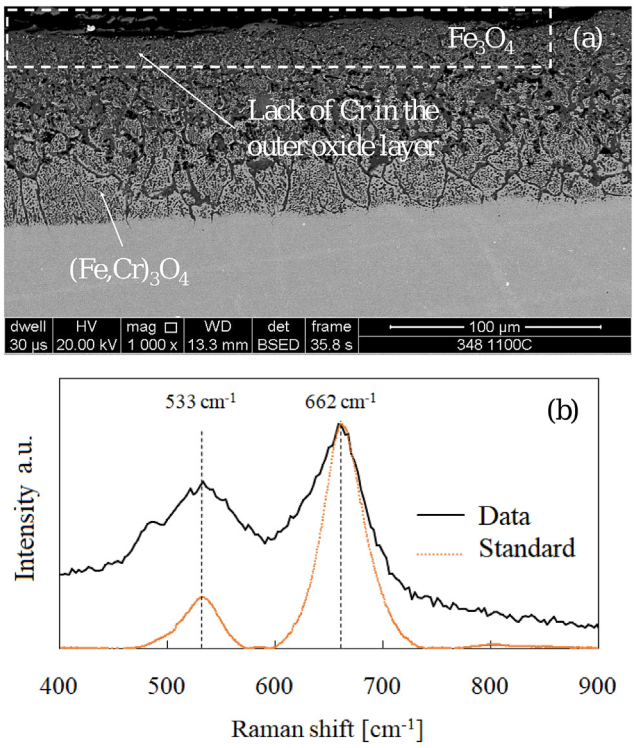

Fig. 11. (a) Cross-section BSE SEM image of AISI 348 specimen after 90 min oxidation at 1100 °C, and (b) Raman spectrum of its magnetite outer layer [4].

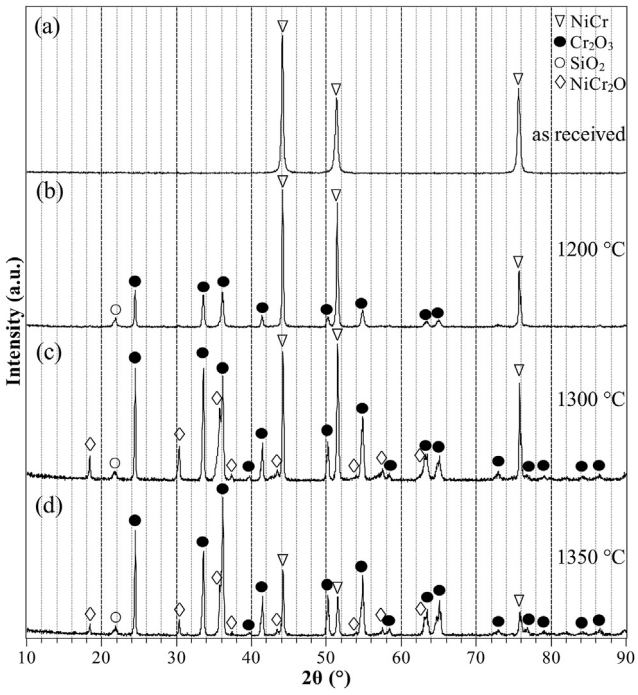

Fig. 12. XRD patterns for Ni–20Cr-1.2Si alloy (a) as received and after 3 h oxidation at (b) 1200 °C, (c) 1300 °C, and (d) 1350 °C.

Consequently, approximately 0.5 kg of hydrogen was generated due to the fast oxidation rates of stainless steel at this temperature range. Therefore, after the onset of severe steam degradation of FeCrAl, a delayed stainless steel case was observed.

Uncertainty of hydrogen generation derived from weight gain curves may arises when the material presents spalling and volatilization [4,6,51], as the formed silica (SiO_2) also undergoes a chemical reaction with water to form a volatile specie, according to the reaction shown in Eq. (17). $Si(OH)_4$ formation and mass transport are also important steps concerning SiC steam oxidation [60]. As Si accounts for less than 2% of alloy mass, hydrogen generated from volatilized Si may not be significant, but Cr_2O_3 layer may also generate hydroxide and volatilize gradually in the form of $CrO_2(OH)_2$ [51], as shown by the chemical reaction in Eq. (18). This uncertainty may be evaluated by measuring hydrogen generation directly from the experiment [6].

$$SiO_{2(s)} + 2H_2O_{(g)} \rightarrow Si(OH)_{4(g)} \quad (17)$$

$$Cr_2O_{3(s)} + 2H_2O_{(g)} + \frac{3}{2}O_{2(g)} \rightarrow 2CrO_2(OH)_{2(g)} \quad (18)$$

The ACTOF presented a series of steam oxidation results of chromium coated samples at high temperatures where systematic differences appear between hydrogen mass and sample mass gain [6]. To correct the effect of chromium(III) oxide volatilization a factor of 1.15 was applied in the numerical calculations, based on the highest noticed difference between hydrogen mass and sample mass gain in ACTOF project [6].

4.3.2. Discussion

High Ni content is not desirable in the core, due to its high thermal neutron capture cross-section, the formation of radioactive Co from $^{58}Ni(n,p)^{58}Co$ reaction with fast neutrons and irradiation-induced helium production of ^{59}Ni [61,62].

Austenitic stainless steels such as AISI 304L and 348, which have lower Ni content, would present a better performance compared to Zr-based alloys [27]. Ni has almost twice the thermal neutron absorption cross-section of Fe [61]. The same parameter for Fe is about 12–16 times higher than that for Zr [63]. Noticeably, there is a trade-off on increasing accident tolerance and worsening neutron transparency.

It is well known that cladding material changes can affect the neutronic performance due to parasitic neutron absorption, consequently impact the cycle length. In order to address the neutron absorption penalty due to different cladding material, a preliminary neutronic assessment was performed considering the NuScale reactor data presented at Table 3. The impact of cladding material change was verified by means of infinite multiplication factor considering a single unit cell calculation using Monte Carlo code Serpent [64]. The infinite multiplication factor gives amount of neutronic reactivity available at the beginning of life considering a specific fuel system. Table 6 presents infinite multiplication factors for different cladding alloys, including the ZIRLO™ (Zr-based alloy) cladding as a reference to comparison. It can be seen that NiCr alloy presents the lowest infinite multiplication factor among others due to high nickel content.

In order to overcome the neutron absorption penalty, changes in fuel rod geometries (pellet diameter, clad thickness, and fuel rod pitch) and/or increase in fuel enrichment degree shall be considered. FeCrAl and NiCr alloys have been studied considering clad thickness of 0.30–0.35 mm [62,65]. One recent literature studied the feasibility of duplex stainless steel for ATF fuel cladding [62]. Moreover, assessment of tritium permeation through the cladding shall be addressed in the future.

The production rate of hydrogen may be increased by injecting water in an overheated core, as it can just lead to the acceleration of degradation [66]. The lower heat from metal-water reaction of Ni-

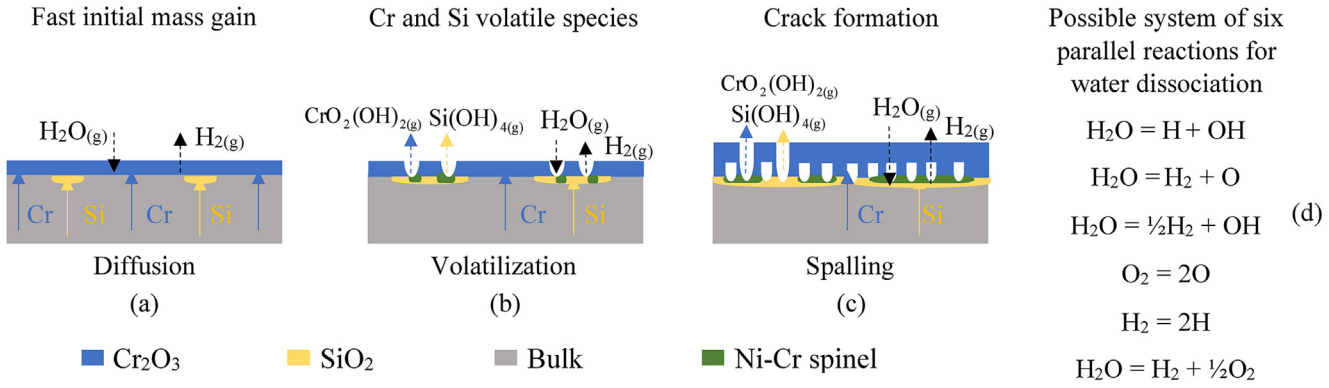

Fig. 13. Schematic short-term oxidation mechanism of Ni–20Cr-1.2Si in high temperature steam presenting three phases: (a) time <20 min: initial diffusion mechanism, (b) time <60 min: volatilization of Cr and Si species, (c) time >60 min: spalling and significant volatilization and (d) possible water dissociation reactions.

Table 5
Main properties and large break LOCA results for Zr-based and ATF cladding materials [26,44,57,58].

Cladding	Start of melting [°C]	Enthalpy of metal-water reaction [kJ/kg alloy]	Time to PCT reach the start of core melting [s]	Generated hydrogen mass [kg]
Zr-based (Zry-4)	1855 [57]	−6527	449	2.82
SS (AISI 348)	1370 [58]	−1059	529	6×10^{-1}
FeCrAl (APMT)	1475 [26]	−2322	686	1×10^{-2}
NiCr (Ni–20Cr–1.2Si)	1345 [44]	−757	543	2×10^{-4}

based and Fe-based alloy may also improve safety margin during core reflood. Thus, by considering ATF cladding, this mitigation measure would not increase hydrogen threat generated during core reflood the short-term of BDBA or design extended conditions.

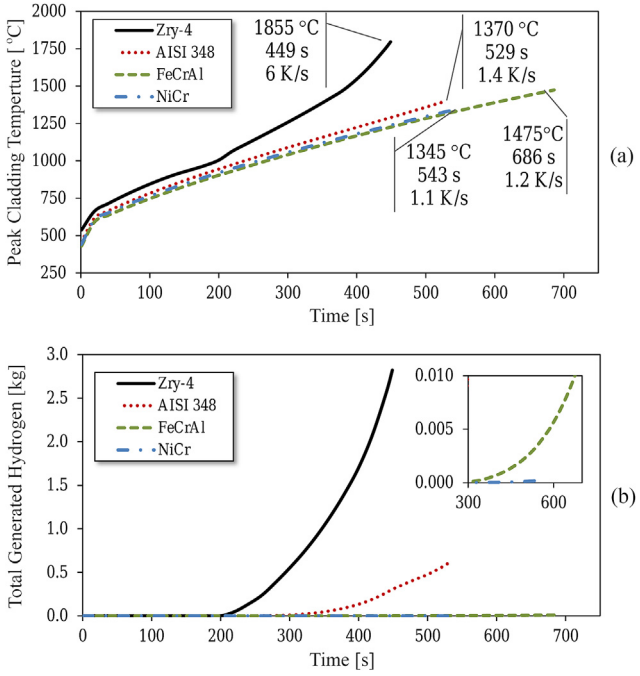

Fig. 14. (a) Peak cladding temperature (PCT) evolution and maximum cladding heat-up rate up to the time where PCT reaches the start of cladding melting temperature (as indicated) and (b) Total generated hydrogen mass for different cladding alloys in LOCA without ECCS scenario (adiabatic boundary conditions).

Table 6
Infinite multiplication factors for different cladding materials (an uncertainty of ±0.0001 should be taken into account at each factor).

Material	Infinite multiplication factor
ZIRLO™	1.3601
FeCrAl	1.2486
AISI 348	1.2357
NiCr	1.1974

ATF claddings are designed to present a better performance in design extension conditions without worsening safety during operational states. In this context, the lack of Fe in the composition might reduce susceptibility to stress corrosion cracking, which make NiCr applicable to pressurized water cooled reactors [65]. NiCr alloy is considered as a promising material for future generations of nuclear reactors [44,50,67]. Furthermore, Ni-based alloy has been applied as structural material due to its exceptional high temperature oxidation resistance and has been proposed for Generation IV core components that will experience temperatures higher than 600 °C [68–70].

5. Conclusions

Fuel cladding design involves a series of constraints regarding fuel performance, neutronic, and mechanical properties under operational and accident conditions. Oxidation resistance plays a major role in nuclear safety at beyond design basis accidents scenarios. A Ni-based alloy containing Si was analysed and compared to other materials, including Zr-based and Fe-based alloys previously investigated [4,26,27]. Negligible amounts of hydrogen were generated from ATF cladding materials up to the start of their melting [26,71]. The conclusions of this paper are as follows:

- A quartic oxidation kinetic model was proposed for short-term Ni–20Cr-1.2Si (wt.%) alloy in steam from 1200 °C to 1350 °C. A

thin oxide scale (up to 20 μm) was observed. It consisted mainly of Cr_2O_3 layer, with an inner SiO_2 layer.
- The investigated NiCr alloy met the proposed accident tolerance criteria, which was previously defined by Ref. [8] as 100x higher oxidation resistance compared to Zr-based alloys in steam at 1200 °C for short times.
- Fe-based and Ni-based alloys at beyond design basis accidents temperatures tend to relocate rather than undergo excessive oxidation. Both would generate less hydrogen during accident progression up to the start of core melting.
- For the same onset time for core uncovery, cladding heat-up rates were significantly lower for Fe-based and Ni-based alloys simulation cases due to their lower absolute enthalpy of metal-water reaction compared to Zr-based alloys. Implying that the enthalpy of metal-water reaction is a key parameter for peak cladding temperature evolution.
- Preliminary neutronic assessment indicates that NiCr cladding would require further reduction in cladding thickness and an increase in fuel enrichment, in order to overcome the reactivity penalty, even when compared to FeCrAl cladding. Thus, further engineering development is necessary aiming to reduce the impact of its neutron absorption penalty.
- A minor Si content seems promising for ATF cladding candidates [56], especially for low-power nuclear power plants and naval reactors in the context of increasing accident tolerance, as SiO_2 reduces the diffusivity of other cations through its layer.

CRediT authorship contribution statement

Alan Matias Avelar: Conceptualization, Methodology, Investigation, Writing – original draft. **Fábio de Camargo:** Investigation, Writing – review & editing. **Vanessa Sanches Pereira da Silva:** Investigation, Writing – review & editing. **Claudia Giovedi:** Conceptualization, Methodology, Writing – review & editing. **Alfredo Abe:** Methodology, Writing – review & editing. **Marcelo Breda Mourão:** Methodology, Writing – review & editing, Supervision.

Declaration of competing interest

The authors declare that they have no known competing financial interests or personal relationships that could have appeared to influence the work reported in this paper.

Acknowledgements

The authors acknowledge the support from CAPES and CNPq and they are grateful to Natalia de Oliveira Souza, Léa Sarita Montagna, Selma Luiza Silva, and Carina Melaré Melchor at AMAZUL and Guilherme Fernandes Nielsen at CTMSP.

References

[1] L.J. Baker, L.C. Just, Studies of metal-water reactions at high temperatures experimental-and theoretical studies of the zirconium-water reaction, in: AEC Research and Development Report, Argonne National Laboratory, Argonne, 1962, https://doi.org/10.2172/4781681. Report No.: ANL-6548).
[2] J.V. Cathcart, R.E. Pawel, R.A. McKee, R.E. Druschel, G.J. Yurek, J.J. Campbell, et al., Zirconium Metal-Water Oxidation Kinetics, IV: Reaction Rate Studies, Oak Ridge National Laboratory, Oak Ridge, 1977, https://doi.org/10.2172/7317596 (Report No.: ORNL/NUREG-17).
[3] V.F. Urbanic, T.R. Heidrick, High-temperature oxidation of Zircaloy-2 and Zircaloy-4 in steam, J. Nucl. Mater. 75 (1978) 251–261, https://doi.org/10.1016/0022-3115(78)90006-5.
[4] A.M. Avelar, C. Giovedi, A.Y. Abe, M.B. Mourão, Oxidation of AISI 304L and 348 stainless steels in water at high temperatures, Mater. Res. 23 (2020), e20200373, https://doi.org/10.1590/1980-5373-MR-2020-0373.
[5] International Atomic Energy Agency – IAEA, Developments in the Analysis and Management of Combustible Gases in Severe Accidents in Water Cooled Reactors Following the Fukushima Daiichi Accident, IAEA, Vienna, 2020 (Report No.: IAEA-TECDOC-1939).
[6] International Atomic Energy Agency – IAEA, Analysis of Options and Experimental Examination of Fuels for Water Cooled Reactors with Increased Accident Tolerance (ACTOF): Final Report of a Coordinated Research Project, IAEA, Vienna, 2020 (Report No.: IAEA-TECDOC-1921).
[7] K.A. Terrani, Accident tolerant fuel cladding development: promise, status, and challenges, J. Nucl. Mater. 501 (2018) 13–30, https://doi.org/10.1016/j.jnucmat.2017.12.043.
[8] B.A. Pint, K.A. Terrani, Y. Yamamoto, L.L. Snead, Material selection for accident tolerant fuel cladding, Metall. Mater. Trans. 2 (2015) 190–196, https://doi.org/10.1007/s40553-015-0056-7.
[9] R.B. Rebak, Versatile oxide films protect FeCrAl alloys under normal operation and accident conditions in light water power reactors, JOM 70 (2018) 176–185, https://doi.org/10.1007/s11837-017-2705-z.
[10] C. Tang, M. Große, S. Ulrich, M. Klimenkov, U. Jäntsch, H.J. Seifert, M. Stüber, M. Steinbrück, High-temperature oxidation and hydrothermal corrosion of textured Cr2AlC-based coatings on zirconium alloy fuel cladding, Surf. Coat. Technol. 419 (2021), 127263, https://doi.org/10.1016/j.surfcoat.2021.127263.
[11] C.R.F. Azevedo, Selection of fuel cladding material for nuclear fission reactors, Eng. Fail. Anal. 18 (2011) 1943–1962, https://doi.org/10.1016/j.engfailanal.2011.06.010.
[12] K.A. Terrani, S.J. Zinkle, L.L. Snead, Advanced oxidation-resistant iron-based alloys for LWR fuel cladding, J. Nucl. Mater. 448 (2014) 420–435, https://doi.org/10.1016/j.jnucmat.2013.06.041.
[13] C.P. Massey, K.A. Terrani, S.N. Dryepondt, B.A. Pint, Cladding burst behavior of Fe-based alloys under LOCA, J. Nucl. Mater. 470 (2016) 128–138, https://doi.org/10.1016/j.jnucmat.2015.12.018.
[14] A. Strasser, J. Santucci, K. Lindquist, W. Yario, G. Stern, L. Goldstein, et al., Evaluation of Stainless Steel Cladding for Use in Current Design LWRs Final Report, 1982 (Report No.: EPRI-NP-2642).
[15] K.A. Unocic, Y. Yamamoto, B.A. Pint, Effect of Al and Cr content on air and steam oxidation of FeCrAl alloys and commercial APMT alloy, Oxid. Met. 87 (2017) 431–441, https://doi.org/10.1007/s11085-017-9745-1.
[16] T.M. Copeland-Johnson, C.K.A. Nyamekye, S.M. Gill, L. Ecker, N. Bowler, E.A. Smith, R.B. Rebak, Characterization of Kanthal APMT and T91 oxidation at beyond design-basis accident temperatures, Corrosion Sci. 171 (2020), 108598, https://doi.org/10.1016/j.corsci.2020.108598.
[17] Y. Qiao, P. Wang, W. Qi, S. Du, Z. Liu, F. Meng, X. Zhang, K. Wang, Q. Li, Z. Yao, C. Bai, X. Wang, Mechanism of Al on FeCrAl steam oxidation behavior and molecular dynamics simulations, J. Alloys Compd. 828 (2020), 154310, https://doi.org/10.1016/j.jallcom.2020.154310.
[18] P.D. Edmondson, S.A. Briggs, Y. Yamamoto, R.H. Howard, K. Sridharan, K.A. Terrani, K.G. Field, Irradiation-enhanced α′ precipitation in model FeCrAl alloys, Scripta Mater. 116 (2016) 112–116, https://doi.org/10.1016/j.scriptamat.2016.02.002.
[19] C. Parisi, Z. Ma, D. Mandelli, N. Anderson, H. Zhang, Risk-informed safety analysis for accident tolerant fuels, Nucl. Sci. Eng. 194 (2020) 748–770, https://doi.org/10.1080/00295639.2020.1732699.
[20] International Atomic Energy Agency – IAEA, Modelling of Fuel Behaviour in Design Basis Accidents and Design Extension Conditions, IAEA, Vienna, 2020 (Report No.: IAEA-TECDOC-1913).
[21] Stuckert J., Grosse M., Steinbrück M. Results of the bundle test QUENCH-19 with FeCrAl claddings. Karlsruher Institut für Technologie (KIT) (Report No.: NUSAFE 3574) http://doi.org/10.5445/IR/1000148370.
[22] C. Kim, C. Tang, M. Grosse, Y. Maeng, C. Jang, M. Steinbrueck, Oxidation mechanism and kinetics of nuclear-grade FeCrAl alloys in the temperature range of 500–1500 °C in steam, J. Nucl. Mater. 564 (2022), 153696 https://www.doi.org/10.1016/j.jnucmat.2022.153696.
[23] S.V. Bechta, E.V. Krushinov, V.I. Almjashev, et al., Phase diagram of the UO2–FeO1+x system, J. Nucl. Mater. 362 (2007) 46–52, https://www.doi.org/10.1016/j.jnucmat.2006.11.004.
[24] J.T. Bittel, L.H. Sjodahl, J.F. White, Oxidation of 304L stainless steel by steam and by air, Corrosion 25 (1969) 7–14, https://doi.org/10.5006/0010-9312-25.1.7.
[25] J. Wang, H. Yeom, P. Humrickhouse, K. Sridharan, M. Corradini, Effectiveness of Cr-coated Zr-alloy clad in delaying fuel degradation for a PWR during a station Blackout event, Nucl. Technol. 206 (2020) 467–477, https://doi.org/10.1080/00295450.2019.1649566.
[26] A. Gurgen, K. Shirvan, Estimation of coping time in pressurized water reactors for near term accident tolerant fuel claddings, Nucl. Eng. Des. 337 (2020) 38–50, https://doi.org/10.1016/j.nucengdes.2018.06.020.
[27] A.M. Avelar, M.B. Mourão, M. Maturana, C. Giovedi, A.Y. Abe, R. Pedrassani, J. Su, On the nuclear safety improvement by post-inerting small modular reactor with stainless steel cladding, Ann. Nucl. Energy 149 (2020), 107775, https://doi.org/10.1016/j.anucene.2020.107775.
[28] Z. Yang, Y. Niu, J. Xue, T. Liu, C. Chang, X. Zheng, Steam oxidation resistance of plasma sprayed chromium-containing coatings at 1200 °C, Mater. Corros. 70 (2019) 37–47, https://doi.org/10.1002/maco.201810156.
[29] E. Kashkarov, B. Afornu, D. Sidelev, M. Krinitcyn, V. Gouws, A. Lider, Recent advances in protective coatings for accident tolerant Zr-based fuel claddings, Coatings 11 (2021) 557, https://doi.org/10.3390/coatings11050557.
[30] D.V. Sidelev, E.B. Kashkarov, M.S. Syrtanov, V.P. Krivobokov, Nickel-chromium

(Ni-Cr) coatings deposited by magnetron sputtering for accident tolerant nuclear fuel claddings, Surf. Coat. Technol. 369 (2019) 69–78, https://doi.org/10.1016/j.surfcoat.2019.04.057.
[31] L.A. Karpyuk, A.M. Savchenko, M. Leont'eva-Smirnova, et al., Steel cladding for VVER fuel pins in the context of accident-tolerant fuel: prospects, Energy 128 (2020) 218–222, https://doi.org/10.1007/s10512-020-00679-3.
[32] V.N. Rechitskii, A.V. Laushkin, V.V. Medkov, Effect of nitrogen on the properties of Bochvalloy (42KhNM) alloy in the operating and high temperature range, Met. Sci. Heat Treat. 51 (2009) 278, https://doi.org/10.1007/s11041-009-9159-z.
[33] J.M. Beeston, Mechanical and Physical Properties of Irradiated Type 348 Stainless Steel, United States, 1980. Report No.: CONF-800609–1), https://inis.iaea.org/search/search.aspx?orig_q=RN:11548494.
[34] S. Han, D.J. Young, Oxidation - nitridation of Ni-Cr-Al alloys, Mater. Res. 7 (1) (2004) 11–16, https://doi.org/10.1590/S1516-14392004000100003.
[35] D.L. Douglass, J.S. Armijo, The effect of silicon and manganese on the oxidation mechanism of Ni-20 Cr, Oxid. Metals 2 (1970) 207–231, https://doi.org/10.1007/BF00603657.
[36] T. Dudziak, L. Boroń, V. Deodeshmukh, J. Sobczak, N. Sobczak, M. Witkowska, W. Ratuszek, K. Chruściel, Steam oxidation behavior of advanced steels and Ni-based alloys at 800 °C, J. Mater. Eng. Perform. 26 (2017) 1044–1056, https://doi.org/10.1007/s11665-017-2535-8.
[37] A.K. Yadav, C.H. Shin, S.U. Lee, H.C. Kim, Experimental and numerical investigation on thermo-mechanical behavior of fuel rod under simulated LOCA conditions, Nucl. Eng. Des. 337 (2018) 51–65, https://doi.org/10.1016/j.nucengdes.2018.06.023.
[38] American Nuclear Society - ANS, Decay Heat Power in Light Water Reactors, ANS, La Grange Park, 2014. Report No.: ANSI/ANS-5.1-2014).
[39] W.G. Luscher, K.J. Geelhood, Material Property Correlations: Comparisons between FRAPCON-3.5, FRAPTRAN-1.5, and MATPRO, Pacific Northwest National Laboratory, Richland, 2014, https://doi.org/10.2172/1030897 (Report No.: NUREG/CR-7024, Rev. 1).
[40] International Atomic Energy Agency - IAEA, Thermophysical Properties of Materials for Water Cooled Reactors, IAEA, Vienna, 1997 (Report No.: IAEA-TECDOC-949).
[41] International Atomic Energy Agency - IAEA, Thermophysical Properties Database of Materials for Light Water Reactors and Heavy Water Reactors - Final Report of a Coordinated Research Project, IAEA, Vienna, 2006 (Report No.: IAEA-TECDOC-1496).
[42] K.G. Field, M.A. Snead, Y. Yamamoto, K.A. Terrani, Handbook on the Material Properties of FeCrAl Alloys for Nuclear Power Production Applications, Oak Ridge: ORNL, 2017, https://doi.org/10.2172/1474581. Report No.: ORNL/TM-2017/186, Rev. 1).
[43] D.T. Hagrman, C.M. Allison, G.A. Berna, SCDAP/RELAP5/MOD 3.1 Code Manual: MATPRO, in: A Library of Materials Properties for Light-Water-Reactor Accident Analysis, vol. 4, USNRC, Washington, 1995, https://doi.org/10.2172/100327 (Report No.: NUREG/CR-6150-Vol.4).
[44] G.V. Kulakov, A.V. Vatulin, S.A. Ershov, et al., Prospects for using chromium-nickel alloy 42KhNM in different types of reactors, Energy 130 (2021) 25–28, https://doi.org/10.1007/s10512-021-00768-x.
[45] K. Monma, H. Suto, H. Oikawa, High-temperature creep of nickel-chromium alloys (on the relation between high-temperature creep and diffusion in nickel base solid solutions, IV), J. Jpn. Inst. Metals 28 (1964) 253–258, https://doi.org/10.2320/jinstmet1952.28.5_253.
[46] Y. Zhong, K. Lan, H. Lee, B. Zhou, Y. Wang, D.K.L. Tsang, J.F. Stubbins, Investigating creep behavior of Ni–Cr–W alloy pressurized tube at 950 °C by using in-situ creep testing system, Nucl. Eng. Technol. 52 (2020) 1481–1485, https://doi.org/10.1016/j.net.2019.12.024.
[47] M. Kvapilova, P. Kral, J. Dvorak, V. Sklenicka, High temperature creep behaviour of cast nickel-based superalloys INC 713 LC, B1914 and MAR-M247, Metals 11 (2021) 52, https://doi.org/10.3390/met11010152.
[48] H. Nickel, F. Schubert, H. Schuster, Evaluation of alloys for advanced high-temperature reactor systems, Nucl. Eng. Des. 78 (1984) 251–265, https://doi.org/10.1016/0029-5493(84)90309-1.
[49] NuScale Power, January, NuScale standard plant design certification application, Chapter Four: Reactor. Available at: https://www.nrc.gov/docs/ML2022/ML20224A492.pdf, 2020.
[50] B.A. Gurovich, A.S. Frolov, D.A. Mal'tsev, S.V. Fedotova, E.A. Kuleshova, Investigation of the possibility of using 42KhNM alloy as a cladding for a tolerant fuel rod, in: Proceedings of the 15th International Scientific-Practical Conference on Atomic Energy, Sevastopol, Russian Federation, 2019. Available at: https://inis.iaea.org/search/search.aspx?orig_q=RN:52045565.
[51] H. Yeom, B. Maier, G. Johnson, T. Dabney, M. Lenling, K. Sridharan, High temperature oxidation and microstructural evolution of cold spray chromium coatings on Zircaloy-4 in steam environments, J. Nucl. Mater. 526 (2019), 151737, https://doi.org/10.1016/j.jnucmat.2019.151737.
[52] J.C. Brachet, E. Rouesne, J. Ribis, T. Guilbert, S. Urvoy, G. Nony, et al., High temperature steam oxidation of chromium-coated zirconium-based alloys: kinetics and process, Corrosion Sci. 167 (2020), 108537, https://doi.org/10.1016/j.corsci.2020.108537.
[53] H.B. Ma, J. Yan, Y.H. Zhao, T. Liu, Q.S. Ren, Y.H. Liao, et al., Oxidation behavior of Cr-coated zirconium alloy cladding in high-temperature steam above 1200 °C, NPJ Mater. Degrad. 5 (2021), https://doi.org/10.1038/s41529-021-00155-8.
[54] J. Zhan, Y. Yang, H. Bi, M. Li, H. Gu, High temperature oxidation behavior of type 444 stainless steel in synthetic automotive exhaust gas, J. Mater. Res. Technol. 12 (2021) 530–541, https://doi.org/10.1016/j.jmrt.2021.03.014.
[55] M. Le Calvar, M. Lenglet, Etude, par spectroscopies optiques de reflexion dans l'ultraviolet, visible, proche infrarouge et infrarouge, par spectroscopie XPS de l'oxydation d'un alliage Ni-20Cr, J. Nucl. Mater. 173 (1990) 71–77, https://doi.org/10.1016/0022-3115(90)90313-C.
[56] A. Leong, Q. Yang, S.W. McAlpine, M.P. Short, J. Zhang, Oxidation behavior of Fe-Cr-1.8Si alloys in high temperature steam, Corrosion Sci. 179 (2021), 109114, https://doi.org/10.1016/j.corsci.2020.109114.
[57] H. Okamoto, O-Zr (Oxygen-Zirconium), J. Phase Equilibria Diffus. 28 (2007) 498, https://doi.org/10.1007/s11669-007-9154-2.
[58] T. Hidayat, D. Shishin, E. Jak, S.A. Decterova, Thermodynamic reevaluation of the Fe–O system, Calphad 48 (2015) 131–144, https://doi.org/10.1016/j.calphad.2014.12.005.
[59] O. Kubaschewski, E.L. Evans, C.B. Alcock, Metallurgical Thermochemistry, Pergamon Press Ltd, New York, 1967.
[60] J.M. Brad, M.B. Shannon, W.H. Paul, Modification of MELCOR for severe accident analysis of candidate accident tolerant cladding materials, Nucl. Eng. Des. 315 (2017) 170–178, https://doi.org/10.1016/j.nucengdes.2017.02.021.
[61] B.A. Pint, K.A. Terrani, M.P. Brady, T. Cheng, J.R. Keiser, High temperature oxidation of fuel cladding candidate materials in steam–hydrogen environments, J. Nucl. Mater. 440 (2013) 420–427, https://doi.org/10.1016/j.jnucmat.2013.05.047.
[62] Q. Xiao, C. Kim, C. Jang, C. Jeong, H. Kim, J. Chen, W. Heo, On the feasibility of duplex stainless steel 2205 as an accident tolerant fuel cladding material for light water reactors, J. Nucl. Mater. 557 (2021), 153265, https://doi.org/10.1016/j.jnucmat.2021.153265.
[63] X. Wu, T. Kozlowski, J.D. Hales, Neutronics and fuel performance evaluation of accident tolerant FeCrAl cladding under normal operation conditions, Ann. Nucl. Energy 85 (2015) 763–775, https://doi.org/10.1016/j.anucene.2015.06.032.
[64] J. Leppänen, M. Pusa, T. Viitanen, V. Valtavirta, T. Kaltiaisenaho, The Serpent Monte Carlo code: status, development and applications in 2013, Ann. Nucl. Energy 82 (2015) 142–150, https://doi.org/10.1016/j.anucene.2014.08.024.
[65] A.M. Savchenko, M.V. Leontieva-Smirnova, G.V. Kulakov, V.N. Rechitsky, Y.V. Konovalov, A.A. Nikitina, Peculiarities of stainless steels application as ATF in VVER'S, in: TopFuel-2018 Conf. Prague, Czech Republic, 2018.
[66] N. Chikhi, N.G. Nguyen, J. Fleurot, Determination of the hydrogen source term during the reflooding of an overheated core: calculation results of the integral reflood test QUENCH-03 with PWR-type bundle, Nucl. Eng. Des. 250 (2012) 351–363, https://doi.org/10.1016/j.nucengdes.2012.05.026.
[67] B.A. Gurovich, A.S. Frolov, I.V. Fedotov, Improved evaluation of ring tensile test ductility applied to neutron irradiated 42XNM tubes in the temperature range of (500 – 1100)°C, Nucl. Eng. Technol. 52 (2020) 1213–1221, https://doi.org/10.1016/j.net.2019.11.019.
[68] P. Xu, L.Y. Zhao, K. Sridharan, T.R. Allen, Oxidation behavior of grain boundary engineered alloy 690 in supercritical water environment, J. Nucl. Mater. 422 (2012) 143–151, https://doi.org/10.1016/j.jnucmat.2011.12.022.
[69] A.F. Rowcliffe, L.K. Mansur, D.T. Hoelzer, R.K. Nanstad, Perspectives on radiation effects in nickel-base alloys for applications in advanced reactors, J. Nucl. Mater. 392 (2009) 341–352, https://doi.org/10.1016/j.jnucmat.2009.03.023.
[70] G.V. Kulakov, Y.V. Konovalov, A.V. Vatulin, et al., High-temperature behavior of irradiated dispersion fuel rods with 42KhNM-alloy cladding, Energy 130 (2022) 208–211, https://doi.org/10.1007/s10512-021-00798-5.
[71] A. Alraisi, Y. Yi, S. Lee, S.A. Alameri, M. Qasem, C. Paik, C. Jang, Effects of ATF cladding properties on PWR responses to an SBO accident: a sensitivity analysis, Ann. Nucl. Energy 165 (2022), 108784, https://doi.org/10.1016/j.anucene.2021.108784.